HHS Public Access

Author manuscript

Ann Nucl Med. Author manuscript; available in PMC 2015 December 02.

Published in final edited form as:

Ann Nucl Med. 2015 December ; 29(10): 877–882. doi:10.1007/s12149-015-1017-z.

Imaging of metastatic clear cell renal cell carcinoma with PSMA-targeted ^{18}F-DCFPyL PET/CT

Steven P. Rowe[1], **Michael A. Gorin**[2], **Hans J. Hammers**[3], **M. Som Javadi**[1], **Hazem Hawasli**[1], **Zsolt Szabo**[1], **Steve Y. Cho**[4], **Martin G. Pomper**[1,3], and **Mohamad E. Allaf**[2]

Mohamad E. Allaf: mallaf@jhmi.edu

[1]The Russell H. Morgan Department of Radiology and Radiological Science, Johns Hopkins University School of Medicine, Baltimore, MD, USA

[2]The James Buchanan Brady Urological Institute and Department of Urology, Johns Hopkins University School of Medicine, 600 North Wolfe Street Park 223, Baltimore, MD 21287, USA

[3]The Department of Medical Oncology at the Sidney Kimmel Comprehensive Cancer Center, Johns Hopkins University School of Medicine, Baltimore, MD, USA

[4]Department of Radiology, University of Wisconsin School of Medicine and Public Health, Madison, WI, USA

Abstract

Objective—Molecular imaging with positron emission tomography (PET) provides a powerful means of identifying and characterizing cancerous processes, as well as providing a quantitative framework within which response to therapy can be ascertained. Unfortunately, the most commonly used PET radiotracer, ^{18}F-fluorodeoxyglucose (FDG), has not demonstrated a definitive role in determining response to therapy in metastatic renal cell carcinoma (RCC). As a result, new radiotracers able to reliably image RCC could be of tremendous value for this purpose.

Methods—Five patients with known metastatic RCC were imaged with the low-molecular weight radiotracer ^{18}F-DCFPyL, an inhibitor of the prostate-specific membrane antigen at 60 min post injection. ^{18}F-DCFPyL PET/ CT and conventional images (either contrast-enhanced computed tomography or magnetic resonance imaging) were centrally reviewed for suspected sites of disease.

Results—In all five patients imaged, sites of putative metastatic disease were readily identifiable by abnormal ^{18}F-DCFPyL uptake, with overall more lesions detected than on conventional imaging. These PET-detected sites included lymph nodes, pancreatic parenchymal lesions, lung parenchymal lesions, a brain parenchymal lesion, and other soft tissue sites. ^{18}F-DCFPyL uptake ranged from subtle to intense with maximum standardized uptake values (SUV_{max}) for the identified lesions of 1.6–19.3. Based upon this small patient series, limited pathology and imaging follow-up of these patients suggests a higher sensitivity for ^{18}F-DCFPyL compared to conventional imaging in the detection of metastatic RCC (94.7 versus 78.9 %).

Correspondence to: Mohamad E. Allaf, mallaf@jhmi.edu.

Compliance with ethical standards: Conflict of interest: The authors report no disclosures relevant to this work.

Conclusions—PSMA expression in the tumor neovasculature of RCC has been previously established and is believed to provide the basis for the imaging findings presented here. PSMA-based PET/CT with radiotracers such as ^{18}F-DCFPyL may allow more accurate staging of patients with RCC and conceivably the ability to predict and follow therapy in patients treated with agents targeting the neovasculature.

Keywords

Prostate-specific membrane antigen (PSMA); Renal cell carcinoma (RCC); Positron emission tomography (PET); DCFPyL

Introduction

Renal cell carcinoma (RCC) is the third most common genitourinary malignancy with more than 60,000 new cases per year diagnosed in the United States alone [1]. In the context of metastatic RCC, definitive assessment of small lesions (i.e., <1 cm) as well as response to systemic therapy can be challenging with currently available anatomic imaging modalities such as contrast-enhanced computed tomography (CT) and magnetic resonance imaging (MRI)[2]. In many non-urologic malignancies, these difficult diagnostic tasks are often performed with the quantitative metabolic information available with ^{18}F-fluorodeoxyglucose (FDG) positron emission tomography (PET)/CT [3]. While ^{18}F-FDG PET/CT can reliably identify sites of metastatic RCC [4], indeterminate lesions are still common and a role for monitoring treatment response has not been clearly established [5].

One characteristic feature of RCC is that sites of disease are highly vascularized, raising the possibility that a PET radiotracer targeting the tumor neovasculature could reliably image metastatic lesions. One potential target for such a radiotracer is the cell surface protein, prostate-specific membrane antigen (PSMA), which, despite the specificity implied by its name, is highly expressed in the tumor neovasculature of a number of solid tumors including a variety of RCC subtypes [6, 7]. The potential utility of imaging of RCC with PSMA-targeted radiotracers was recently demonstrated in a single case report of a patient with metastatic clear cell RCC (ccRCC) [8]. Herein, we expand upon this initial case by reporting data on a series of 5 patients with metastatic ccRCC who were successfully imaged with the ^{18}F-labeled low-molecular weight PSMA ligand 2-(3-{1-carboxy-5-[(6-[18F]fluoro-pyridine-3-car-bonyl)-amino]-pentyl}-ureido)-pentanedioic acid, more commonly known as ^{18}F-DCFPyL [9].

Materials and methods

Five patients were prospectively recruited to participate in this study between April and June 2015 (selected demographic information is included in Table 1). The study protocol was approved by our hospital's Institutional Review Board, and patients were imaged following informed consent under a Food and Drug Administration exploratory investigational new drug application (eIND 108943). All patients had previously undergone a radical nephrectomy for a diagnosis of ccRCC and at the time of ^{18}F-DCFPyL PET/CT had findings on conventional imaging (i.e., contrast-enhanced CT or MRI) compatible with recurrent/

metastatic disease. All patients were naïve to systemic therapy at the time of ^{18}F-DCFPyL PET/CT.

The chemistry and radiochemistry necessary for the synthesis of ^{18}F-DCFPyL have been previously described [10]. Patients were kept nil per os for at least 6 h prior to radiotracer administration. One hour after injection of ≤333 MBq (≤9 mCi) of ^{18}F-DCFPyL, patients were asked to void and then were positioned supine for imaging. PET/ CT scans were performed on a Discovery DRX PET/CT scanner (GE Healthcare, Waukesha, WI) with CT-derived attenuation correction. A whole body CT was first obtained from the mid-thighs through the vertex of the skull [120 kVp, 80 mA maximum (auto-adjusting)] followed by PET acquisition in 3D emission mode performed at 4 min per bed position. The acquired PET images were reconstructed using a standard clinical ordered subset expectation maximization (OSEM) algorithm.

^{18}F-DCFPyL PET/CT, diagnostic CT, and MRI studies were analyzed using Mirada Medical XD Software (Mirada Medical, Oxford, UK). The body CT and MRI scans were reviewed by a body imaging subspecialist (H.H.) who was blinded to all clinical and PET/CT data. ^{18}F-DCFPyL PET studies were also blindly reviewed by experienced nuclear medicine readers (S.P.R. and M.S.J.), with PET positive sites selected based on visual uptake higher than adjacent background. The single brain MRI from this patient cohort was not centrally reviewed, with the clinical interpretation being used for comparison.

Results

Overall, 29 lesions were identified on at least one modality. Table 2 lists the sites of lesions detected with either conventional imaging or ^{18}F-DCFPyL PET/CT, with those lesions visible on only one imaging modality indicated by italics. Conventional imaging identified 18 lesions suspicious for metastatic ccRCC (range 1–9 per patient, Table 2). In contrast, ^{18}F-DCFPyL PET/CT was able to identify 28 sites of abnormal radiotracer avidity (range 1–14 per patient, Table 2), 17 of which corresponded to sites of disease on conventional imaging. The only lesion that ^{18}F-DCFPyL was unable to identify was a 6-mm metastatic lesion in segment II of the liver (patient #1). It is likely that both the small size of this lesion and the background radiotracer uptake in the liver prevented adequate evaluation by PET. In contrast, ^{18}F-DCFPyL PET/CT identified small lymph nodes in the mediastinum and retroperitoneum that were too small to adequately characterize with conventional imaging, as well as possible bone metastases that were completely occult. Additionally, abnormal ^{18}F-DCFPyL uptake was noted in sites that would be rare for metastatic involvement with RCC including the paraspinal musculature and the perineal subcutaneous soft tissues.

A maximum intensity projection (MIP) image of a patient with multiple sites of disease is shown in Fig. 1. The normal biodistribution of ^{18}F-DCFPyL can also be appreciated in Fig. 1, with significant uptake present in the lacrimal and salivary glands, liver, kidneys, proximal small bowel, segments of the left ureter, and bladder (see Ref. [10] for detailed biodistribution and dosimetry with this radiotracer). Notably, in this patient cohort, ^{18}F-DCFPyL PET/CT was able to identify sub-centimeter lymph nodes (Fig. 2) and subtle bone

lesions (Fig. 3) that were not definitively assessed with conventional imaging. Metastatic lesions with detectable ^{18}F-DCFPyL uptake also included pancreatic masses (Fig. 4) and small lung nodules (Fig. 5). A single patient with a brain metastasis was also found to have uptake in that lesion (Fig. 6). The range of lean body mass corrected maximum standardized uptake values (SUV_{max}) for all sites of disease was 1.6–19.3, corresponding to moderate to intense uptake visually.

Following imaging with ^{18}F-DCFPyL PET/CT, one patient (patient #3 in Tables 1, 2) proceeded to right adrenalectomy and a site of metastatic RCC was confirmed by surgical pathology. Patients #1, #2, and #4 were started on tyrosine kinase inhibitor therapy, while patient #5 received high-dose interleukin-2. Patient #2 was also treated with stereotactic ablative radiotherapy to the right frontal lobe lesion. Except for patient #3, follow-up imaging with CT or MRI was available for all patients within 3 months of ^{18}F-DCFPyL PET/CT. Of the 29 lesions originally noted on conventional imaging and/or ^{18}F-DCFPyL PET/CT, five lesions demonstrated progression at follow-up, 13 showed a response to therapy (including multiple lymph nodes that had been too small to characterize on conventional imaging but nonetheless decreased further in size at follow-up), and 10 were either not re-imaged, could not be appreciated on the follow-up imaging, or remained unchanged. Based upon these very preliminary results, and considering only those lesions for which pathologic proof is available or progression/response to therapy were present on imaging, the sensitivity of ^{18}F-DCFPyL PET/CT was 94.7 % while the sensitivity for conventional imaging was 78.9 %. Given the lack of known false positives with either modality, specificities cannot be calculated.

Discussion

Based on the results of this pilot study, ^{18}F-DCFPyL PET/ CT appears to be a highly sensitive imaging modality for the detection of metastatic ccRCC in a diverse number of anatomic sites including the bone, brain, lymph nodes, soft tissue, and abdominal viscera. In aggregate, these results suggest that ^{18}F-DCFPyL PET/CT may have a clinically useful role in the evaluation of patients with ccRCC and indeterminate findings on conventional imaging. Common examples of such findings include retroperitoneal and mediastinal lymph nodes measuring <1 cm in short axis as well as pulmonary nodules. Often the clinician must follow these lesions for some period of time awaiting growth to confirm the suspicion of metastatic disease. Imaging with a putatively more sensitive modality such as ^{18}F-DCFPyL PET/CT may, therefore, allow for improved staging and more timely detection of disease, with initiation of systemic therapy or site-directed treatment such as stereotactic ablative radiotherapy if indicated.

Beyond improving upon the sensitivity of conventional cross-sectional imaging, ^{18}F-DCFPyL offers the possibility of being used as a functional imaging agent to measure and/or predict response to agents that target the tumor neovasculature (e.g., tyrosine kinase inhibitors and bevacizumab [11]) by providing an in vivo readout of neovascular density in these lesions. Because ^{18}F-DCFPyL binds to endothelial cells within the tumor microenvironment [6, 7], higher pre-treatment levels of radiotracer uptake may identify lesions that are more likely to respond to neovasculature-targeting therapies. Further,

changes in radiotracer uptake may precede appreciable changes in lesion size on anatomic imaging, aiding in the assessment of treatment response.

The major limitation of this study is that pathologic proof of disease at the sites of ^{18}F-DCFPyL uptake is lacking except for an isolated adrenal lesion that was resected and found to be metastatic RCC. As detailed above, conventional imaging follow-up (CT or MRI) is available for a number of lesions, many of which responded to therapy consistent with the behavior of metastases. However, longer term clinical and imaging follow-up will be necessary to absolutely determine the nature of lesions that are not amenable to pathologic diagnosis. In particular, those lesions that have no conventional imaging correlate (e.g., the T3 vertebral body lesion in Fig. 3) cannot be targeted for biopsy and can only be confirmed on the basis of eventual progression.

Ultimately, the utility of PSMA-based PET imaging with radiotracers such as ^{18}F-DCFPyL in the assessment of patients with metastatic ccRCC will need to be addressed with larger prospective trials, though the results of this pilot study are highly encouraging.

Acknowledgments

We acknowledge funding from the Prostate Cancer Foundation Young Investigator Award, EB006351, CA134675, CA184288, CA103175, and CA183031. We thank Aki-mosa Jeffrey-Kwanisai and Yavette Morton for clinical trial coordination. We thank Takahiro Higuchi, M.D., Ph.D. for critical evaluation of the manuscript.

References

1. Siegel RL, Miller KD, Jemal A. Cancer statistics, 2015. CA Cancer J Clin. 2015; 65:5–29. [PubMed: 25559415]
2. Brufau BP, Cerqueda CS, Villalba LB, Izquierdo RS, González BM, Molina CN. Metastatic renal cell carcinoma: radiologic findings and assessment of response to targeted therapy by using multidetector CT. Radiographics. 2013; 33:1691–716. [PubMed: 24108558]
3. Wahl RL, Jacene H, Kasamon Y, Lodge MA. From RECIST to PERCIST: evolving considerations for PET response criteria in solid tumors. J Nucl Med. 2009; 50(Suppl 1):122S–50S. [PubMed: 19403881]
4. Wang HY, Ding HJ, Chen JH, Chao CH, Lu YY, Lin WY, et al. Meta-analysis of the diagnostic performance of [^{18}F]FDG-PET and PET/CT in renal cell carcinoma. Cancer Imaging. 2012; 12:464–74. [PubMed: 23108238]
5. Calderella C, Muoio B, Isgrò MA, Porfiri E, Treglia G, Gio-vanella L. The role of fluorine-18-fluorodeoxyglucose positron emission tomography in evaluating the response to tyrosine-ki-nase inhibitors in patients with metastatic primary renal cell carcinoma. Radiol Oncol. 2014; 48:219–27. [PubMed: 25177235]
6. Chang SS, O'Keefe DS, Bacich DJ, Reuter VE, Heston WD, Gaudin PB. Prostate-specific membrane antigen is produced in tumor-associated neovasculature. Clin Cancer Res. 1999; 5:2674–81. [PubMed: 10537328]
7. Baccala A, Sercia L, Li J, Heston W, Zhou M. Expression of prostate-specific membrane antigen in tumor-associated neovas-culature of renal neoplasms. Urology. 2007; 70:385–90. [PubMed: 17826525]
8. Demirci E, Ocak M, Kabasakal L, Akyel R, Nematyazar J, Aygun A, et al. ^{68}Ga-PSMA PET/CT imaging of metastatic clear cell renal cell carcinoma. Eur J Nucl Med Mol Imaging. 2014; 41:1461–2. [PubMed: 24756358]
9. Chen Y, Pullambhatla M, Foss CA, Byun Y, Nimmagadda S, Senthamizhchelvan S, et al. 2-(3-{1-Carboxy-5-[(6-[^{18}F]fluoro-pyridine-3-carbonyl)-amino]-pentyl}-ureido)-pentanedioic acid,

[^{18}F]DCFPyL, a PSMA-based PET imaging agent for prostate cancer. Clin Cancer Res. 2011; 17:7645–53. [PubMed: 22042970]

10. Szabo Z, Mena E, Rowe SP, Plyku D, Nidal R, Eisenberger MA, et al. Initial evaluation of [18F]DCFPyL for prostate-specific membrane antigen (PSMA)-targeted PET imaging of prostate cancer. Mol Imaging Biol. 2015; 17:565–74. [PubMed: 25896814]
11. Shuch B, Amin A, Armstrong AJ, Eble JN, Ficarra V, Lopez-Beltran A, et al. Understanding pathologic variants of renal cell carcinoma: distilling therapeutic opportunities from biologic complexity. Eur Urol. 2015; 67:85–97. [PubMed: 24857407]
12. Heng DY, Xie W, Regan MM, Warren MA, Golshayan AR, Sahi C, et al. Prognostic factors for overall survival in patients with metastatic renal cell carcinoma treated with vascular endothelial growth factor-targeted agents: results from a large multicenter study. J Clin Oncol. 2009; 27:5794–9. [PubMed: 19826129]

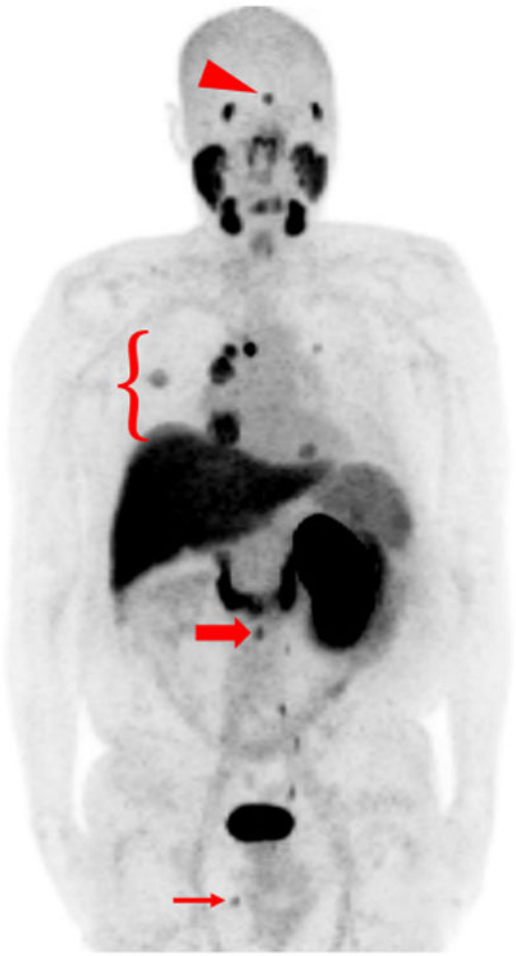

Fig. 1.

MIP image of patient #2 who was status post-right nephrec-tomy with multiple sites of metastatic disease. Normal radiotracer uptake is noted in the lacrimal glands, salivary glands, oropharynx, nasopharynx, liver, spleen, proximal small bowel, left kidney, left ureter, and bladder. Abnormal sites of uptake include a brain lesion (*red arrowhead*), lung nodules as well as mediastinal and hilar lymph nodes (*red bracket*), a retroperitoneal lymph node (*thick red arrow*), and a soft tissue perineal lesion (*thin red arrow*) (color figure online)

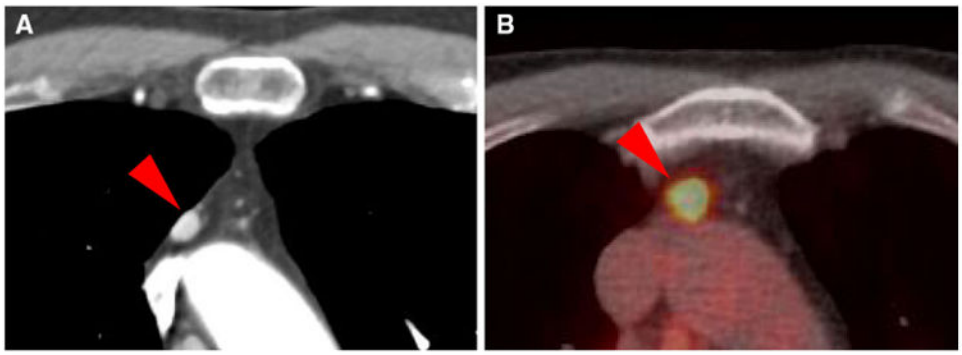

Fig. 2.

4-mm intensely radiotracer-avid anterior mediastinal lymph node (SUV_{max} 19.3) from patient #2, as demonstrated on contrast-enhanced CT (**a**) and ^{18}F-DCFPyL PET/CT (**b**) (*arrowheads*)

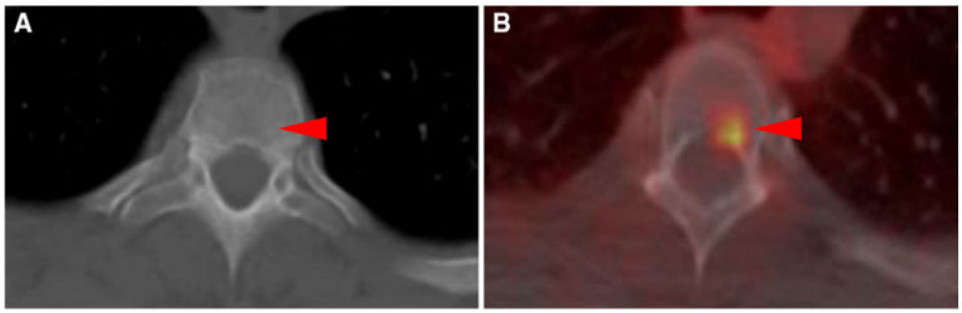

Fig. 3.

T3 vertebral body bone lesion from patient #5 which was occult on contrast-enhanced CT of the chest (**a**), but demonstrated moderate radiotracer uptake (SUV_{max} 2.6) when imaged with ^{18}F-DCFPyL PET/CT (**b**) (*arrowheads*)

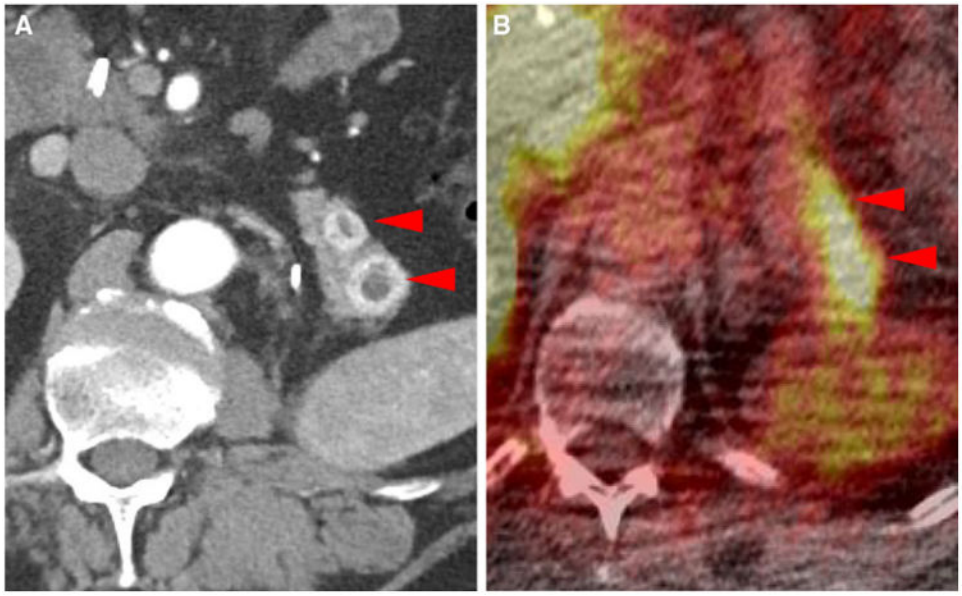

Fig. 4.

Metastatic lesions to the pancreatic tail in patient #1 (SUV_{max} 5.0 in the more anterior lesion and SUV_{max} 7.4 in the more posterior lesion) as noted on contrast-enhanced CT (**a**) and ^{18}F-DCFPyL PET/CT (**b**) (*arrowheads*)

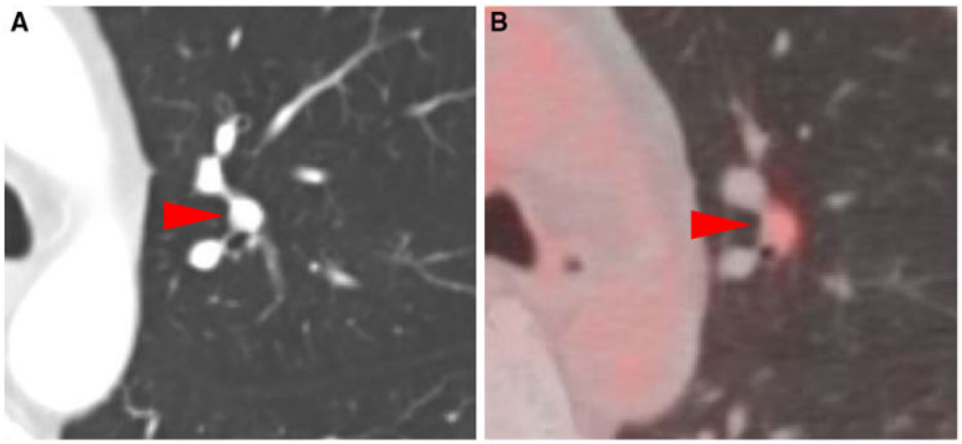

Fig. 5.

Subtle radiotracer uptake (SUV_{max} 1.7) in a small lung nodule (1 cm in diameter) as seen on contrast-enhanced CT (**a**) and ^{18}F-DCFPyL PET/CT (**b**) (*arrowheads*) in patient #2

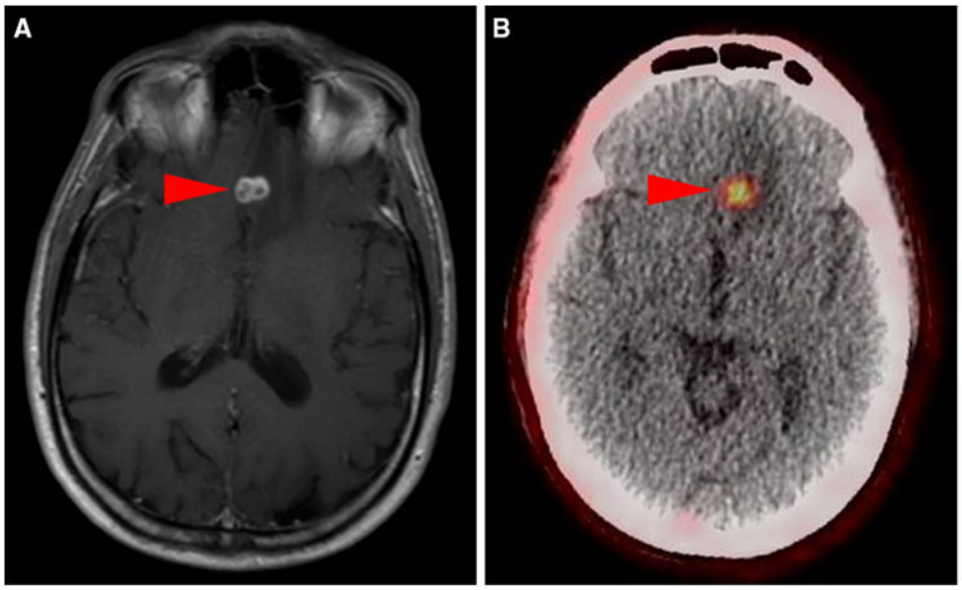

Fig. 6.

Axial contrast-enhanced T1-weighted MRI of the brain (**a**) and ^{18}F-DCFPyL PET/CT (**b**) from patient #2 demonstrating an intensely ^{18}F-DCFPyL-avid (SUV_{max} 3.9) brain lesion in the left frontal lobe (*arrowheads*)

Table 1

Study cohort characteristics

Patient #	Age (years)	Sex	TNM stage at initial diagnosis	Nephrectomy histology	Time from nephrectomy to metastasis (months)	Heng criteria prognostic group [12]
1	65	Male	pT2a cN0M0	ccRCC, grade II	73	Favorable risk
2	61	Male	pT3aN1M1	ccRCC, grade III[a]	0	Poor risk
3	54	Male	pT1b cN0M0	ccRCC, grade III	11	Intermediate risk
4	47	Male	pT2a cN0M0	ccRCC, grade III	16	Intermediate risk
5	58	Male	pT1bN0M1	ccRCC, grade II	0	Intermediate risk

[a]Biopsy of site of metastatic disease consistent with sarcomatoid ccRCC

Table 2

Lesions detected on conventional imaging and ^{18}F-DCFPyL PET/CT

Patient #	Sites of lesions identified on conventional imaging (CT or MRI)	Sites of lesions identified on ^{18}F-DCFPyL PET/CT
1	Paraesophageal lymph node, posterior mediastinal lymph node, *liver segment II*, anterior pancreatic tail, posterior pancreatic tail	Paraesophageal lymph node, posterior mediastinal lymph node, anterior pancreatic tail, posterior pancreatic tail
2	Left frontal lobe, superior and inferior right hilar lymph nodes, left upper lobe lung nodule, right posterior mediastinal lymph node, right upper lobe lung mass, left lower lobe mass, pancreatic body, pancreatic tail	Left frontal lobe, *right paraspinal muscle*, *right paratracheal lymph node*, *anterior mediastinal lymph node*, superior and inferior right hilar lymph nodes, left upper lobe lung nodule, right posterior mediastinal lymph node, right upper lobe lung mass, pancreatic body, pancreatic tail, left lower lobe mass, *aortocaval lymph node*, *perineal subcutaneous soft tissue*
3	Right adrenal gland	Right adrenal gland
4	Left hilar lymph node	Left hilar lymph node
5	Posterior left iliac bone, posterior right iliac bone	*Right T2 transverse process*, *T3 vertebral body*, *right humerus*, *posterior left rib 9*, posterior left iliac bone, posterior right iliac bone, *anterior left iliac bone*, *left proximal femur*

Italicized sites indicate lesions not identified on the comparison modality